Huge influence of hydrogenation on the magnetic properties and structures of the ternary silicide NdMnSi

Sophie Tencé, Gilles André, Etienne Gaudin, Pierre Bonville, Adel F. Al Alam, Samir F. Matar, Wilfried Hermes, Rainer Pöttgen, Bernard Chevalier

To cite this version:

Sophie Tencé, Gilles André, Etienne Gaudin, Pierre Bonville, Adel F. Al Alam, et al.. Huge influence of hydrogenation on the magnetic properties and structures of the ternary silicide NdMnSi. Journal of Applied Physics, 2009, 106 (3), 033910 (13 p.). 10.1063/1.3190488 . hal-00418918

HAL Id: hal-00418918
https://hal.science/hal-00418918

Submitted on 6 Mar 2024

JOURNAL OF APPLIED PHYSICS **106**, 033910 (2009)

Huge influence of hydrogenation on the magnetic properties and structures of the ternary silicide NdMnSi

S. Tencé,[1,2] G. André,[2] E. Gaudin,[1] P. Bonville,[3] A. F. Al Alam,[1] S. F. Matar,[1]
W. Hermes,[4] R. Pöttgen,[4] and B. Chevalier[1,a)]
[1]*CNRS, Université de Bordeaux, ICMCB, 87 Avenue du Dr. A. Schweitzer, 33608 Pessac Cedex, France*
[2]*CEA, IRAMIS, LLB, 91191 Gif-Sur-Yvette Cedex, France*
[3]*CEA, IRAMIS, SPEC, 91191 Gif-Sur-Yvette Cedex, France*
[4]*Institut für Anorganische und Analytische Chemie, Westfälische Wilhelms-Universität Münster, Corrensstraße 30, 48149 Münster, Germany*

(Received 22 December 2008; accepted 2 July 2009; published online 12 August 2009)

The hydride NdMnSiH obtained by exposure of the ternary silicide NdMnSi under a pressure of 4 MPa of hydrogen at 523 K crystallizes in the tetragonal ZrCuSiAs-type structure where H atom occupies the tetrahedral $[\mathrm{Nd}_4]$ sites. The hydrogenation of NdMnSi induces an increase in the unit cell volume close to 3.3%. The investigation of NdMnSiH by magnetization and specific heat measurements reveals the existence of two antiferromagnetic ordering, respectively, at $T_{N1}=565(5)$ K and $T_{N2}=103(4)$ K. Neutron powder diffraction shows that these Néel temperatures are associated with an antiferromagnetic arrangement of the (i) Mn substructure (T_{N1}) and (ii) Nd substructure linked to a reorientation of the Mn one (T_{N2}). Comparison of the T_{N1} and T_{N2} temperatures of NdMnSiH to those reported for the initial compound NdMnSi indicates a strong increase in T_{N1} ($280\ \mathrm{K} \rightarrow 565\ \mathrm{K}$) and a significant decrease in T_{N2} ($185\ \mathrm{K} \rightarrow 103\ \mathrm{K}$). The magnetic properties, magnetic structures, and values of Nd and Mn ordered magnetic moments are discussed using both band structure calculations and comparison with the behaviors of other ternary silicides and germanides based on manganese and rare earth elements. © *2009 American Institute of Physics*. [DOI: 10.1063/1.3190488]

I. INTRODUCTION

Within the past decade, many phosphide RE*T*PO and arsenide RE*T*AsO oxides, where RE is a rare earth and *T* a transition metal such as Mn, Fe, Co, Ni, and Ru, were synthesized.[1–4] These compounds crystallize in the tetragonal ZrCuSiAs-type structure (space group $P4/nmm$). The oxygen atoms are surrounded by four rare earth neighbors in tetrahedral arrangement $[\mathrm{RE}_4]$ whereas the environment of a phosphorus or arsenic atom consists of a square antiprism $[\mathrm{RE}_4T_4]$ formed by four rare earth and four transition metal atoms.[1] In other words, this structure can be described by a stacking along the *c*-axis of two layers formed by $[\mathrm{RE}_4T_4]$ antiprisms and separated by one layer of $[\mathrm{RE}_4]$ tetrahedral units where O^{2-} anion is inserted. Recent investigations of these phosphide oxides revealed interesting superconducting properties. For instance, magnetization and electrical resistivity measurements performed on LaFePO (Refs. 5–7) and LaNiPO (Refs. 8 and 9) show, respectively, low superconducting temperatures at 3.2 and 4.3 K. This discovery on the iron- and nickel-based compounds has involved an intensive effort of the research community in order to explore this promising superconducting family. In particular, in 2008 it was reported that the doping of LaFeAsO,[10,11] CeFeAsO,[12] NdFeAsO,[13] and SmFeAsO (Ref. 14) with F^- anion at the O^{2-} site induces an increase in superconducting temperatures, respectively, at 26, 41, 50, and 43 K. Moreover, the synthesis of oxygen-deficient arsenic oxides $\mathrm{NdFeAsO}_{1-y}$ using high-pressure technique reveals the existence of a superconducting phase having $\mathrm{NdFeAsO}_{0.6}$ as chemical formula and 53–54 K as critical temperature.[15] Electronic structure calculations of these superconducting materials performed, for instance, on LaFePO (Ref. 6) or PrZnPO (Ref. 16) suggest two types of chemical bonding: one is covalent in the LaO or PrO and FeP or ZnP layers and the second rather ionic between the layers.

Our recent works devoted to the hydrogenation of ternary equiatomic compounds RE*TX*(X=Si or Ge), crystallizing in the tetragonal CeFeSi-type structure, show that it is possible to insert hydrogen in the $[\mathrm{RE}_4]$ tetrahedral site without changing the initial space group symmetry.[17–23] The resulting hydrides RE*TX*H are stable in ambient conditions and adopt, like the phosphide RE*T*PO or arsenide RE*T*AsO oxides, the tetragonal ZrCuSiAs-type structure;[24] along the *c* axis, two layers of $[\mathrm{RE}_4T_4]$ antiprisms hosting Si or Ge atoms are separated by one layer of $[\mathrm{RE}_4]$ tetrahedral units inserting H atoms. Moreover, the H absorption induces an anisotropic expansion of the unit cell parameters: *a* decreases while *c* increases strongly, which involves an expansion of the unit cell volume. On the contrary to the phosphide or arsenide oxides where the parent ternary compounds RE*TX* (X=P or As) do not exist, the family of RE*TX*H hydrides allows to study the influence of hydrogenation on the physical properties of the RE*TX* (X=Si or Ge) intermetallics. In particular, it is interesting to compare the type of the RE–H chemical bonding to that of RE–O observed in phosphide or arsenide oxides.

[a)] Author to whom correspondence should be addressed. Tel.: +33-5-4000-6336. Fax: +33-5-4000-2761. Electronic mail: chevalie@icmcb-bordeaux.cnrs.fr.

0021-8979/2009/106(3)/033910/13/$25.00

The role of hydrogenation was recently determined for several cerium-based ternary equiatomic compounds such as CeCoSi,[18,20,21] CeCoGe,[17,20,21] and CeRuSi.[22,23] The effect of hydrogenation on the magnetic properties is very different according to the nature of the T transition metal in the compound. Hydrogen absorption by CeCoSi and CeCoGe induces a transition from antiferromagnetic to spin fluctuation behavior whereas a transition heavy-fermion behavior → antiferromagnetism is evidenced by hydrogen insertion into CeRuSi. In order to explain these different transitions, the calculation of the electronic structures and of the chemical bonding properties of CeCoSi,[18] CeRuSi,[25] and their hydrides using the covalent bond energy was performed. This analysis suggests the following: (i) in the hydride CeCoSiH, the presence of strong Ce–H bonding, which leads to a demagnetization of cerium, prevails over the cell expansion effect, which tends to stabilize the trivalent cerium, and (ii) a decrease in the Ce–H bonding in CeRuSiH. The strength of the Ce–H bonding is correlated with the value of the Ce–H interatomic distance which increases from 2.391 to 2.447 Å in the sequence CeCoSiH → CeRuSiH.[18,22]

Motivated by these various results, we have investigated the hydrogenation of the REMnSi compounds crystallizing in the CeFeSi-type structure. This series of equiatomic ternary silicides presents a particularity since the Mn and RE substructures exhibit a magnetic ordering at different temperatures and their magnetic structures are strongly influenced by the arrangement of these two substructures.[26] Also, the Mn substructure orders around room temperature. Hydrogenation is likely to induce changes in both magnetic substructures due to the modifications of the exchange interactions correlated with the crystal structure evolution. Among the REMnSi compounds, the ternary silicide NdMnSi presents an antiferromagnetic behavior below $T'_{N1}=280$ K corresponding to the Mn ordering whereas the Nd substructure orders antiferromagnetically at $T'_{N2}=185$ K, these temperatures being determined using neutron powder diffraction.[26] Moreover, a third transition occurs near 80 K which corresponds to a spin reorientation of the Mn substructure connected to a strong magnetostriction effect involving a symmetry change from tetragonal to orthorhombic.

Now, we have prepared the hydride NdMnSiH. We report here on its investigation by magnetization and specific heat measurements and also by neutron powder diffraction. Then, the magnetic properties and structures of the hydride are discussed and compared to the ones of pristine NdMnSi. This comparison is performed on the basis of first principles of the electronic structures of NdMnSi and its hydride, which enables the description of the electronic and magnetic structures as well as the bonding characteristics.

II. EXPERIMENTAL PROCEDURES AND CALCULATION

A polycrystalline NdMnSi sample was synthesized by arc melting a stoichiometric mixture of the pure elements (purity above 99.9%) in a high-purity argon atmosphere. Then, the sample was turned and remelted several times to ensure homogeneity. Annealing was done for 1 month at 1073 K by enclosing the sample in an evacuated quartz tube. Its x-ray powder pattern (Cu $K\alpha$ radiation) is completely indexed on the basis of a tetragonal unit cell with the CeFeSi type. No parasitic phase is detected. The unit cell parameters deduced from this investigation agree with those reported previously.[26]

Hydrogen absorption experiments were performed using the apparatus described previously.[27] An annealed ingot of NdMnSi was heated under vacuum at 523 K for 12 h and then exposed to 4 MPa of hydrogen gas at the same temperature. The amount of H atoms inserted, determined volumetrically by monitoring pressure changes in a calibrated volume, is one per NdMnSi mole. Also, the H absorption induces a decrepitation into small grains of the starting ingot and it can be noted that the formed hydride is stable at room temperature in air or under vacuum.

Magnetization measurements were performed using a superconducting quantum interference device magnetometer in the temperature range 5–300 K and in applied fields up to 4.8 T. In the high-temperature range from 300 to 630 K, the susceptibility was measured with the oven option of a Quantum Design Physical Properties Measurement System (PPMS). Therefore for these measurements, the sample was glued to the sample holder with an alumina-based cement. Heat capacity measurements were realized on the initial ternary silicide NdMnSi and its hydride by a relaxation method with a Quantum Design PPMS system and using a two tau model analysis. A piece (12–20 mg) of the sample was glued on the sample holder using Apiezon N grease and data were taken between 1.8 and 350 K.

Neutron powder diffraction experiments were performed at the Orphée reactor (CEA/Saclay, France) on the two-axis diffractometer G4.1 ($\lambda=2.4226$ Å; 800 cell-position-sensitive detector). Several patterns were recorded between 1.4 and 307 K in a cryostat and between 300 and 580 K in a furnace. The data were analyzed using the Rietveld profile method by means of the FULLPROF program,[28] with neutron-scattering lengths and magnetic form factors of Mn and Nd atoms taken, respectively, from Refs. 29 and 30.

The electronic and magnetic structure calculations of NdMnSi and its hydride were performed within the density functional theory framework[31,32] using the scalar relativistic augmented spherical wave (ASW) method.[33,34] All valence states were treated as band states. In the minimal ASW basis set, the outermost shells were chosen to represent the valence states using partial waves up to $l_{\max}+1=4$ for Nd and $l_{\max}+1=3$ for Mn and Si. The completeness of the valence basis set was checked for charge convergence, i.e., less than 0.1 electrons for $l_{\max}+1$. The self-consistent field calculations were run to a convergence of 10^{-8} for the charge density and the accuracy of the method is in the range of about 10^{-8} Ry (1 Ry=13.6 eV) regarding energy differences. The effects of exchange and correlation were treated based on the local density approximation (LDA).[35] With four f-electrons for Nd, the 4f-subshell is only partially filled. From this, the single particle scheme of the LDA or generalized gradient approximation is good enough as we have recently shown in Ce-based systems.[36] This is with respect to the possibility of calling for the introduction of a Coulomb on site repulsion parameter within extra LDA+U/GGA+U based calculations.[37] Such preliminary calculations were carried out to check this point. They showed only a small departure from the single particle picture, e.g., for the lowering of the $4f$ density of states (DOS) at the Fermi level, pushing it down in energy.

The computational procedure follows a protocol through which a nonmagnetic (NM) configuration is first assumed, meaning that spin degeneracy is imposed for all valence states with equal spin occupations; these calculations are also called non-spin-polarized (NSP). Such a configuration should not be confused with that of a paramagnet, which could be simulated either by supercell calculations with random spin orientations on atoms or by calling for disordered local moment approaches based on the coherent potential approximation[38] or the LDA+dynamic mean field theory scheme.[39] NM computations are relevant at two levels, allowing an analysis of the partial atom projected densities of states (PDOSs) at the Fermi level with respect to magnetic instability and assessing the chemical bonding. Then spin polarized (SP) calculations with different initial spins, majority spins (↑) and minority spins (↓), can lead at self-consistency either to finite or zero local moments within an implicit long-range ferromagnetic (FM) order. Antiferromagnetic (AFM) calculations are also done to identify the ground state for both systems based on energy differences especially starting from the FM energies. This is done here by defining half of the atomic constituents as up spin aligned and the other half as down spin aligned within a single cell as well as by using a supercell with a doubling along the c axis.

The analysis of the chemical bonding pertains to the information on the nature of the interactions between the atomic constituents. From electronic structure calculations this can be obtained from examining the crystal orbital overlap population (COOP) introduced by Hoffmann[40] in extended Hückel-type calculations and later on implemented within the ASW code. In short hand notation avoiding extended equations, the COOP can be looked at as the DOS weighted by the overlap integral S_{ij} between two chemical species i and j. They carry the same unit as the DOS of inverse energy (1/eV). In the plots, positive, negative, and zero magnitudes of COOP are indicative of bonding, antibonding, and nonbonding interactions, respectively. Further a mapping of the electron localization within the structure will be obtained for better illustration. Here we use the electron localization function (ELF) introduced by Becke and Edgecombe.[41] It allows determining the amount of localization of electrons with respect to the free electron gas distribution whence its normalization. The dimensionless ELF magnitude ranges from 0 to 1 with ELF=1/2 corresponding to the free electron gas distribution, while the extreme cases of zero and full localization correspond to 0 and 1, respectively. All calculations were carried out using the experimental findings presented below.

III. RESULTS

A. Magnetization and specific heat

The temperature dependence of the magnetization M divided by the applied magnetic field $\mu_0 H$ for the hydride NdMnSiH is plotted in Fig. 1. In the high-temperature region [Fig. 1(a)], the $M/\mu_0 H(T)$ curve exhibits a shoulder around $T_{N1}=565(5)$ K, which suggests the occurrence of a long-range magnetic order below T_{N1}. Above this temperature, the $M/\mu_0 H(T)$ curve seems to follow a Curie–Weiss law but the lack of paramagnetic data (because the hydride starts to lose hydrogen above 630 K) does not allow the accurate determination of the paramagnetic parameters, mainly the effective magnetic moment. Below 200 K, the $M/\mu_0 H(T)$ curve displays two other particularities [Fig. 1(b)]: a very weak bump at $T_{N2}=100-122$ K where the derivative shows a very broad minimum [inset of Fig. 1(b)] and another shoulder at $T_{N3}=34(2)$ K. The magnetization measurements presented here for the hydride NdMnSiH are very different to those reported previously for NdMnSi.[26] For this latter ternary silicide, the $M(T)$ curve obtained for $\mu_0 H=1$ T shows a maximum at $T'_{N2}=175$ K and a pronounced shoulder near $T'_{N3}=80$ K. Using neutron diffraction investigation, these ordering temperatures were attributed, respectively, to the AFM ordering of the Nd substructure (but $T'_{N2}=185$ K in this investigation) and to the spin reorientation of the Mn substructure (T'_{N3}). In

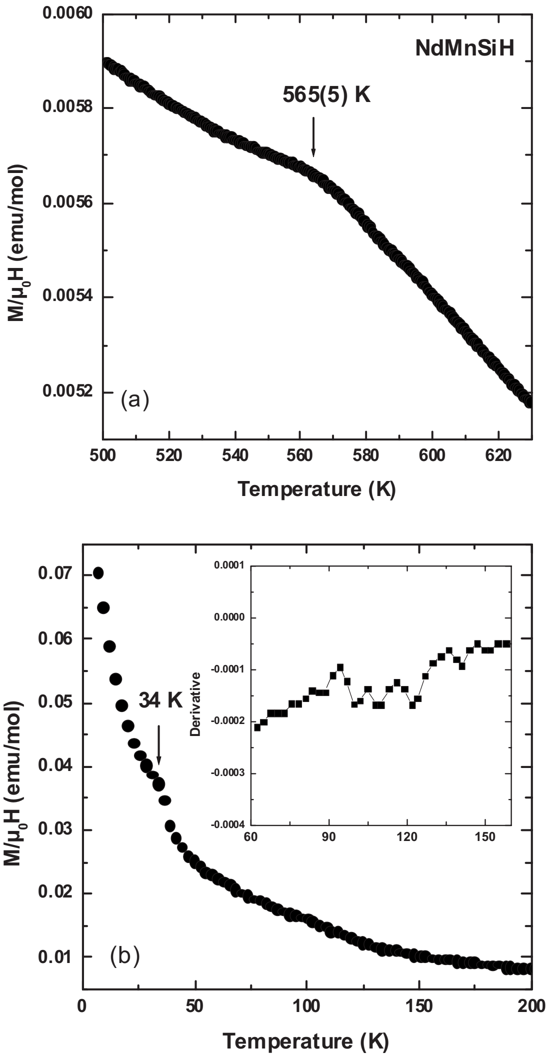

FIG. 1. Temperature dependence of the magnetization M divided by the applied magnetic field ($\mu_0 H=1$ T) for the hydride NdMnSiH at temperatures (a) between 500 and 630 K and (b) below 200 K (the inset presents the thermal dependence of the derivative between 60 and 160 K).

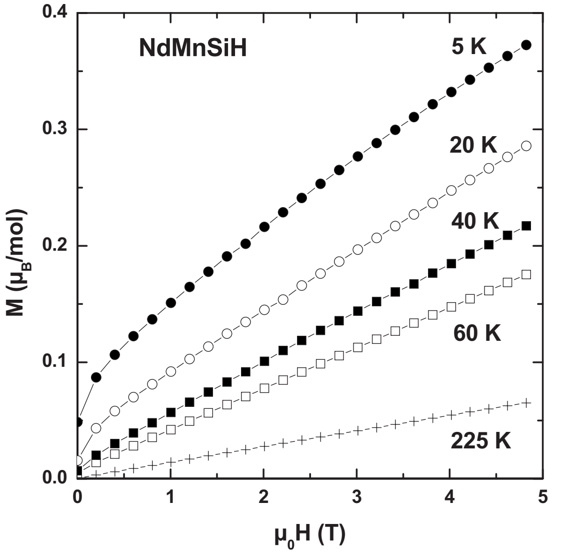

FIG. 2. Field dependence at selected temperatures of the magnetization for the hydride NdMnSiH.

this study, the AFM ordering of the Mn substructure occurring at $T'_{N1}=280$ K was not detected by magnetization measurement. Finally, the comparison of the $M(T)$ curves obtained for NdMnSi and its hydride suggests a great influence of the hydrogenation on the magnetic properties of the initial ternary silicide.

Magnetic isotherms recorded for NdMnSiH at selected temperatures are shown in Fig. 2. These measurements were made with decreasing field strengths, first at 225 K then at decreasing temperatures. The linear field dependence for the 225 K isotherm suggests that the magnetic ordering existing between T_{N1} and T_{N2} presents an AFM behavior. The magnetic isotherms between T_{N2} and T_{N3}, for instance, at 60 and 40 K, exhibit a very small curvature. Moreover, below 40 K, the magnetic isotherms reveal clearly the presence of a remanence for the hydride; for instance, the remanence is of $0.05\mu_B$ mol^{-1} at 5 K. This result suggests the presence of a weak FM component at low temperatures.

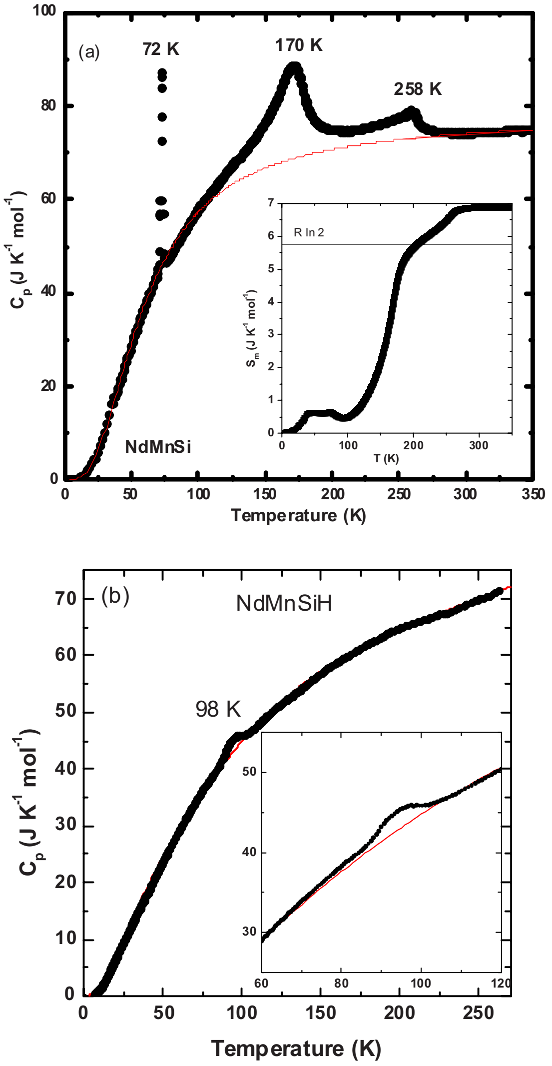

FIG. 3. (Color online) Temperature dependence without applied magnetic field of the specific heat of (a) NdMnSi and (b) NdMnSiH. For NdMnSi, the solid line (in red) is the fit of the C_e+C_l contributions by the Debye model and the inset presents an estimation of the thermal dependence of the magnetic entropy. For NdMnSiH, a zoom of the peak corresponding to the ordering of the Nd substructure is represented in the inset and the solid red line is the fit (Debye–Einstein model) to estimate the C_e+C_l contributions.

The specific heats C_p of NdMnSi and its hydride have been measured at zero magnetic field (Fig. 3). For NdMnSi, the curve $C_p(T)$ [Fig. 3(a)] clearly exhibits three peaks: two broad at 258 and 170 K and a narrow and sharp peak at 72 K. These three temperatures, defined by the maximum of the peaks, are associated with the occurrence of the three magnetic transitions detected for NdMnSi by neutron powder diffraction.[26] The two broad peaks point out the AFM ordering of the Mn and Nd substructures, respectively, and the sharp peak at 72 K corresponds to the spin reorientation of the Mn substructure connected to the structural transition from tetragonal to orthorhombic symmetry with decreasing temperature (first-order change). According to the Dulong–Petit law, the limiting heat capacity at high temperature for a compound with n atoms per mole is expected to be $3nR$, where R is the gas constant. For NdMnSi the limiting value of the lattice heat capacity C_l should be 75 J K^{-1} mol^{-1} ($n=3$) which agrees with the experimental data of 74 J K^{-1} mol^{-1}. This means that the main contribution to C_p at room temperature is the lattice C_l contribution. In order to extract the magnetic contribution C_m, $C_p(T)$ data were analyzed using the Debye model to estimate the C_l contribution added to the electronic contribution C_e. So, we used the following formula:

$$C_e + C_l = \gamma T + 9nR\left(\frac{T}{\theta_D}\right)^3 \int_0^{\theta_D} \frac{x^4 e^x}{(e^x-1)^2}dx,$$

where θ_D is the Debye temperature and γ the Sommerfield coefficient. We obtained a good fit, represented by the solid thin line in Fig. 3(a), with $\theta_D=241$ K and $\gamma=5.7$ mJ K^{-1} mol^{-1}, which are typical parameters for such metallic compounds. The C_m contribution to $C_p(T)$ was calculated as the difference $C_m=C_p-(C_e+C_l)$. The magnetic entropy change S_m is then estimated using the relation $S_m(T)=\int_0^T(C_m(T)/T)dT$. The temperature dependence of S_m [inset of Fig. 3(a)] shows that the magnetic ordering of the Nd substructure ($T'_{N2}=170$ K) is associated with a large jump of about 5.3 J K^{-1} mol^{-1}. This is much lower than the

$R \ln 10 = 19.1$ J K^{-1} mol^{-1} value corresponding to $R \ln(2J+1)$ with $J=9/2$ and close to the $R \ln 2 = 5.76$ J K^{-1} mol^{-1} value expected for a doublet ground state ($J=1/2$). This suggests that the magnetic contribution is probably underestimated considering the high value of T'_{N2}. It is noteworthy that the second jump at higher temperature corresponds to the Mn ordering transition.

Below 270 K, the curve $C_p(T)$ of the hydride NdMnSiH depicted in Fig. 3(b) shows only a small peak at 98 K which can be associated with the magnetic ordering appearing at T_{N2}. On the contrary, no anomaly is observed at $T_{N3} = 34(2)$ K. For this hydride, the C_p value at 270 K, 72 J K^{-1} mol^{-1}, is weaker than the Dulong–Petit limit which should be 100 J K^{-1} mol^{-1}. Nevertheless, the saturation in the $C_p(T)$ curve is not reached yet and so we cannot conclude about the Dulong–Petit law. The use of the same procedure as the one described above for NdMnSi to estimate the lattice and electronic contributions did not lead to a good fit of the experimental data. Indeed, as often in hydrides, a Debye model is not sufficient to describe accurately the C_l contribution. We have thus added Einstein's modes in C_l in order to take into account the optic phonons modes in C_l. We found a good agreement between the experimental data and a Debye–Einstein model with two Einstein modes: $C_l + C_e = 1/3(C_{\text{Debye}} + C_{\text{Einstein1}} + C_{\text{Einstein2}}) + \gamma T$. This fit gives the following parameters: $\theta_D = 155$ K, $\gamma = 35$ mJ K^{-1} mol^{-1}, $\theta_{E1} = 372$ K, and $\theta_{E2} = 1884$ K. The magnetic specific heat C_{mag} and the magnetic entropy change are then calculated as described previously for NdMnSi. We found a jump of entropy of 0.54 J K^{-1} mol^{-1} at T_{N2} which is lower than the estimated value for NdMnSi and lower than the $R \ln 2$ value expected for quasidoublet ground state.

B. Neutron powder diffraction

1. Crystal structure of NdMnSiH

Analysis of the neutron diffraction pattern of NdMnSiH recorded at 307 K shows that this hydride adopts the tetragonal ZrCuSiAs-type structure ($P4/nmm$ space group) deriving from that of CeFeSi (NdMnSi). No trace of any impurity phase was detected in the pattern. The unit cell parameters are $a = 4.0260(2)$ Å and $c = 7.8139(4)$ Å at 307 K. Thus, the hydrogenation of NdMnSi induces a strong anisotropic expansion of the unit cell since a decreases weakly from 4.103(2) (Ref. 26) to 4.0260(2) Å (−1.9%) while c increases strongly from 7.284(5) (Ref. 26) to 7.8139(4) Å (+7.3%). This is accompanied by an increase in the unit cell volume (+3.3%). The best Rietveld profile refinement, obtained with the reliability factors $R_{wp} = 8.7\%$ and $R_{B\text{-nucl}} = 2.6\%$, gives as positional parameters Nd 2c-site [1/4 1/4 $z_{\text{Nd}} = 0.661(1)$], Mn 2a-site (3/4 1/4 0), Si 2c-site [1/4 1/4 $z_{\text{Si}} = 0.188(1)$], and H 2b-site (1/4 3/4 1/2) (Table I). These last values indicate, in particular, that the atomic position of Si is strongly affected by H insertion into NdMnSi: z_{Si} varies from 0.206(2) (Ref. 26) to 0.188(1). On the contrary, z_{Nd} is almost not affected by the H insertion since it varies from 0.666(2) (Ref. 26) to 0.661(1). It is worth pointing out that the hydrogenation of CeRuSi induces the same tendency for the structural modifications.[23] According to our data, the H atoms are inserted unambiguously in the 2b-site empty in NdMnSi with an occupancy of 0.99(2). The main refined crystal parameters at 578 K are also given in Table I despite the very low statistics.

TABLE I. Main refined parameters for NdMnSiH at various temperatures (G4.1 data).

$T=578$ K	$T=307$ K	$T=1.4$ K
$a=4.029(1)$ Å	$a=4.0260(2)$ Å	$a=4.0227(3)$ Å
$c=7.886(1)$ Å	$c=7.8139(4)$ Å	$c=7.7844(5)$ Å
$z_{\text{Nd}}=0.658(2)$	$z_{\text{Nd}}=0.661(2)$	$z_{\text{Nd}}=0.660(1)$
$z_{\text{Si}}=0.188(4)$	$z_{\text{Si}}=0.188(1)$	$z_{\text{Si}}=0.189(1)$
occ.(H)=1.00(5)	occ.(H)=0.99(2)	occ.(H)=1
$R_{B\text{-nucl}}=4.1\%$	$R_{B\text{-nucl}}=2.6\%$	$R_{B\text{-nucl}}=2.5\%$
	$\mu_{\text{Mn}}=2.61(5)\mu_B$	$\mu_{\text{Mn}}=2.80(5)\mu_B$
	$\theta_{\text{Mn}}=30(5)°$	$\mu_{\text{Nd}}=1.88(5)\mu_B$
	$R_{B\text{-mag}}=2.4\%$	$\theta_{\text{Mn}}=90°$
		$R_{B\text{-mag}}=2.8\%$

Table II compares the interatomic distances existing in NdMnSi and its hydride. The distances $d_{\text{Nd–H}} = 2.374(5)$ Å are comparable to that reported for the hydride NdH_2 (2.368 Å) where H atoms occupy also the tetrahedral [Nd_4] sites.[42] The hydrogenation of NdMnSi induces a decrease in the $d_{\text{Mn–Mn}}$ distances (−1.9%); in NdMnSiH, these distances [2.8467(2) Å] are close to those observed for the ternary silicide $NdMn_2Si_2$ ($d_{\text{Mn–Mn}} = 2.833$ Å),[43] which exhibits an AFM ordering of the Mn substructure below $T_N = 381$ K.[44] As the magnetic properties of the Mn substructure is strongly influenced by the intralayer $d_{\text{Mn–Mn}}$ distance, this steric consideration suggests a great modification of the Néel temperature in the sequence NdMnSi → NdMnSiH. On the contrary, the $d_{\text{Nd–Mn}}$ distances increase strongly (+4.6%) during the H insertion into NdMnSi. Certainly, the magnetic coupling between the Nd and Mn substructures decreases in the hydride. Finally, the intralayer [4.0260(2) Å] and interlayer [3.799(7) Å] $d_{\text{Nd–Nd}}$ distances are influenced differently by the hydrogenation, one decreases (−1.9%) whereas the other increases weakly (+0.6%).

TABLE II. Interatomic distances (Å) in NdMnSi (Ref. 26) and NdMnSiH at room temperature. The standard deviations calculated by the FULLPROF program are given between brackets. In general, the real error is estimated by multiplying the standard deviation by a factor between 2 and 3 (Ref. 60).

		NdMnSi	NdMnSiH
Nd	4H		2.374(4)
	4Si	3.090	3.082(5)
	4Mn	3.182	3.327(6)
	1Si	3.482	3.69(1)
	4Nd	3.777	3.799(7)
	4Nd	4.103	4.0260(2)
Mn	4Si	2.467	2.492(6)
	4Mn	2.901	2.8467(2)
	4Nd	3.182	3.327(6)
	2H		3.9070(2)
Si	4Mn	2.467	2.492(6)
	4Nd	3.090	3.082(5)

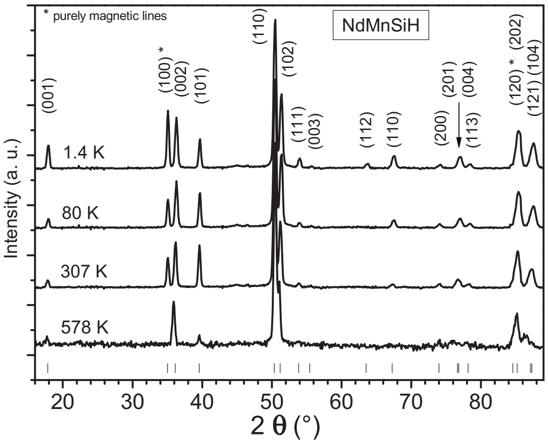

FIG. 4. Selected neutron diffraction patterns of NdMnSiH. The Miller indices are given and the ticks correspond to 2θ-Bragg positions for the nuclear and magnetic cells. The purely magnetic reflections are not allowed by extinction rules for the crystallographic structure in the $P4/nmm$ space group.

2. Magnetic structures of NdMnSiH

Several neutron diffraction patterns were recorded between 578 K, above the magnetic transition at $T_{N1}=565$ K, and 1.4 K (Fig. 4). At 578 K, only nuclear diffraction peaks are distinguished (reflection conditions; $hk0$: $h+k=2n$ and $h00$: $h=2n$). The best refinement at 578 K is depicted in Fig. 5 and the refined parameters are given in Table I. Below T_{N1}, for instance, at 307 K, additional peaks as (100) appear in the patterns; they are characteristic of an AFM ordering of the Mn substructure, in agreement with the magnetization measurements. The peaks can all be indexed on the basis of the nuclear unit cell [i.e., with a propagation vector $\mathbf{k}=(0,0,0)$] which means that the peak intensities result from a nuclear contribution and a magnetic one. The best refinement at 307 K (pattern with the best statistics) leads to a Mn-magnetic moment making an angle of $\theta=30(5)°$ with the c-axis and having as value $2.61(5)\mu_B$ mol^{-1} (Table I and Fig. 5). At 100 K, the saturation of the Mn-magnetic moment is reached with a value of $2.81(5)\mu_B$ mol^{-1}. The magnetic structure of NdMnSiH for $T>T_{N2}$ is drawn in Fig. 6(a). It consists of a stacking of AFM (001) Mn planes, the Mn moments being ferromagnetically coupled with their direct neighbors situated in each adjacent plane along the c-axis. The temperature dependence of the Mn moment, presented in Fig. 7, leads to an estimated Néel temperature of $T_{N1}=555(10)$ K, in good agreement with the AFM temperature determined from the susceptibility measurement [$T_{N1}=565(5)$ K]. It can be noted that this Mn-magnetic arrangement exhibits many similarities with that reported for the ternary silicide LaMnSi,[26] but in this case the direction of the Mn-magnetic moment makes an angle of $\theta=45(1)°$ with the c-axis.

Below 100 K, some changes occur (Fig. 4): the (101) line decreases, and besides, some peaks start to grow up as line (001) one. The decrease in the (101) magnetic intensity clearly results from a moment reorientation of the Mn substructure which corresponds to a rocking of the Mn-magnetic moment in the basal plane (a,b). The second observation is the sign of the presence of an ordered magnetic moment for Nd which becomes significant below 100 K. For instance, the growth of the (001) line clearly shows the occurrence of a Nd-magnetic moment in the basal plane (a,b). Indeed, for the AFM Mn substructure, the magnetic structure factor of the (001) line is given by $F(001)_{\mathrm{Mn}} \propto M_1+M_2$ where M_1 and M_2 are the Mn moments lying in $z=0$, with $M_1=-M_2$, yield-

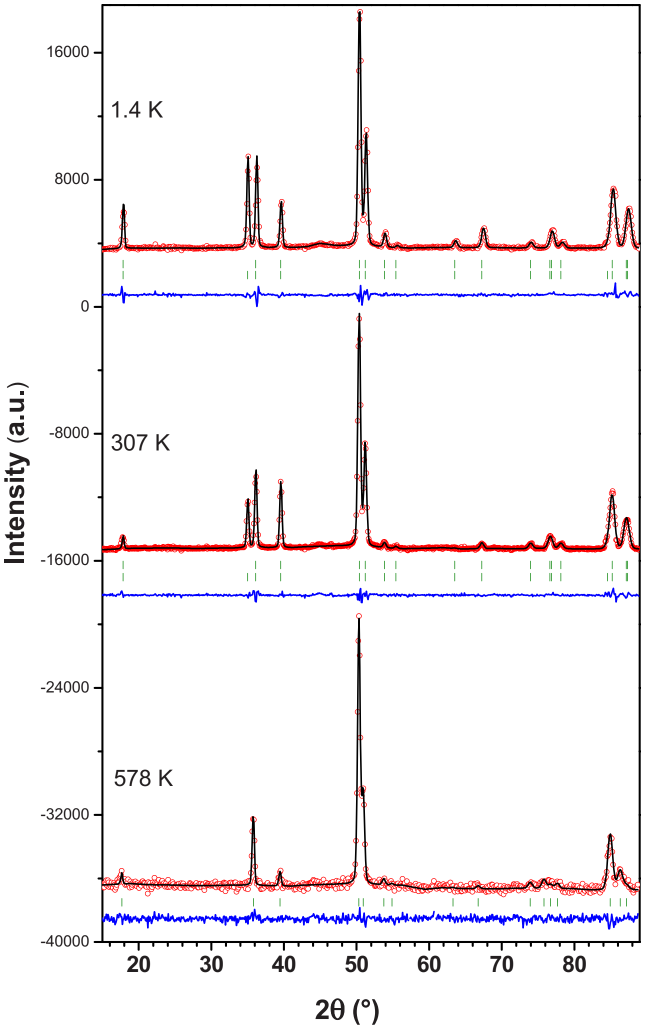

FIG. 5. (Color online) Rietveld profile refinement of NdMnSiH at 1.4 K ($R_{B\text{-nucl}}=2.5\%$, $R_{B\text{-mag}}=2.8\%$), 307 K, and 578 K (low counting time). The open circles represent the observed data points and the solid lines reveal the calculated profile and the difference (bottom) between the observed and calculated profiles. The ticks correspond to 2θ-Bragg positions.

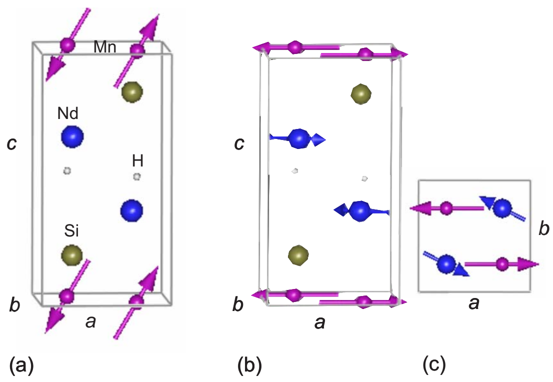

FIG. 6. (Color online) Magnetic structure of NdMnSiH at (a) 307 K (Mn substructure) and 1.4 K (b) with its projection in the basal plane (c) (Nd and Mn substructures).

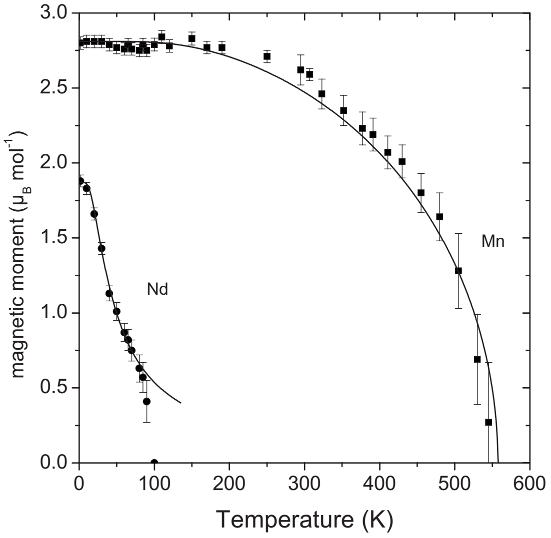

FIG. 7. Temperature dependence of the Mn and Nd magnetic moments in NdMnSiH (error bars are given by the magnetic refinement). The solid lines are the fits using the Brillouin function.

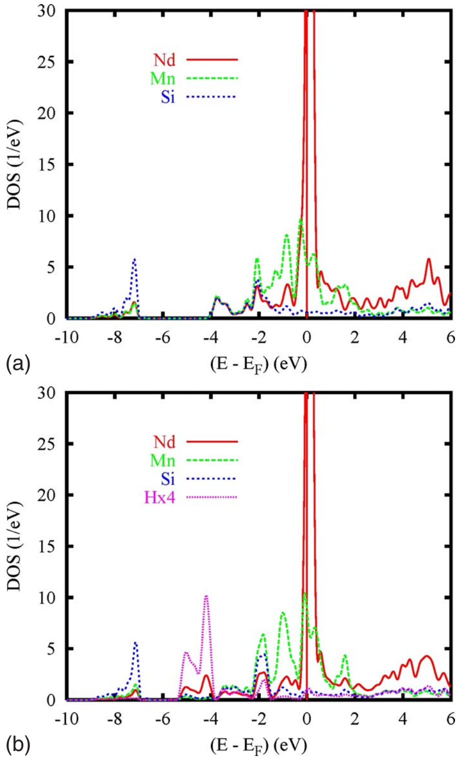

FIG. 8. (Color online) NM site PDOS for (a) NdMnSi and (b) NdMnSiH. The H PDOS were artificially multiplied by 4 for the sake of clarity.

ing $F(001)_{\mathrm{Mn}}=0$. On the contrary, for the Nd substructure, the magnetic structure factor is given by $F(001)_{\mathrm{Nd}} \propto M_1' e^{2i\pi z} + M_2' e^{2i\pi(1-z)}$ where M_1' and M_2' are the Nd moments in $z \approx 0.661$ and $1-z$, respectively, with $M_1' = -M_2'$ (AFM arrangement), yielding $F(001)_{\mathrm{Nd}} \propto iM_1' \sin(2\pi z) \neq 0$. The best refinement at 1.4 K (Fig. 5) leads to an AFM arrangement of the Nd moments with a main component along the same direction as the Mn moments (*a*-axis, for instance) and a weaker component perpendicular to the main one (*b*-axis). A significant Nd FM component is excluded because it would imply the growth of some peaks which is not observed. At 1.4 K, the magnetic structure, depicted in Figs. 6(b) and 6(c), is formed by a stacking of AFM Mn planes separated by two FM Nd layers of opposite magnetization. The Mn and the Nd moments are both in the basal plane and the Nd moment direction makes an angle of $\theta' = 27(4)°$ with the Mn one. If we assume that the Mn moments lie along the *a*-axis, the Nd moments are coupled with their nearest Mn atoms in two different ways: antiferromagnetically coupled in the planes $x=1/4$ and 3/4 and ferromagnetically coupled in the planes $y=1/4$ and 3/4. The moment values at 1.4 K are $1.88(5)\mu_B$ for Nd and $2.80(5)\mu_B$ for Mn ($R_{B\text{-mag}}=2.8\%$) (Table I). The Nd moment value is smaller than that expected for the free Nd^{3+} ion ($3.27\mu_B$) which may be explained by the crystal field effect or/and the occurrence of $4f$-d hybridization as observed in some compounds based on neodymium and transition metal.[45] The temperature dependence of the Nd moment is depicted in Fig. 7 and it shows that this moment vanishes near 100(5) K as Néel temperature of the Nd substructure. Thus, the weak bump displayed by the $M/\mu_0 H(T)$ curve around 100–122 K [Fig. 1(b)] and the peak near 98 K in the $C_p(T)$ curve [Fig. 3(b)] seem to correspond to the Nd-substructure ordering linked to a reorientation of the Mn substructure in the basal plane (a,b). It is interesting to notice that the Nd ordering in $\mathrm{NdMn_2Si_2}$ (Ref. 44) or in $\mathrm{NdMnSi_2}$ (Ref. 46) also occurs simultaneously with the Mn moment reorientation process. In NdMnSiH, the thermal evolutions of both Nd AFM components seem to show a smooth rotation of the Nd moment into the basal plane between 20 and 50 K from 27(4)° to 45(7)°. This reorientation process could explain the small anomaly observed in the $M/\mu_0 H(T)$ curve at $T_{N3}=34(2)$ K. Nevertheless, we notice that 34 K is the FM ordering temperature of $\mathrm{NdMn_2Si_2}$.[44] But the presence of this phase in our sample is not detected by the x-ray and neutron powder diffractions. We also notice that the small FM component seen in the magnetic isotherms below 40 K (Fig. 2) is not observed by neutron diffraction which is possible if this component is too weak ($<0.2\mu_B$). As a consequence, a slight canting in the AFM ordering of the Nd or the Mn substructure likely occurs.

C. Electronic and magnetic structure calculations

These calculations were performed with the methodology presented above in Sec. II. At self-consistent convergence little charge transfer was observed between the atoms for NdMnSi and its hydride. In such compounds, it can be rather argued that the quantum mixing between the different valence states of the constituents is the underlying mechanism of bonding as it will be explicated from the PDOS, the analysis of the chemical bonding based on overlap populations, as well as the ELF maps.

1. Nonmagnetic calculations

In Fig. 8, showing the PDOS for NdMnSi and its hydride, the Fermi level (E_F) is taken as zero energy. This is also done in the following plots describing the chemical bonding. A major feature of a large DOS at E_F, $n(E_F)$, is observed in both compounds for the $4f$(Nd) states whose major part lies above E_F. The latter observation can be ex-

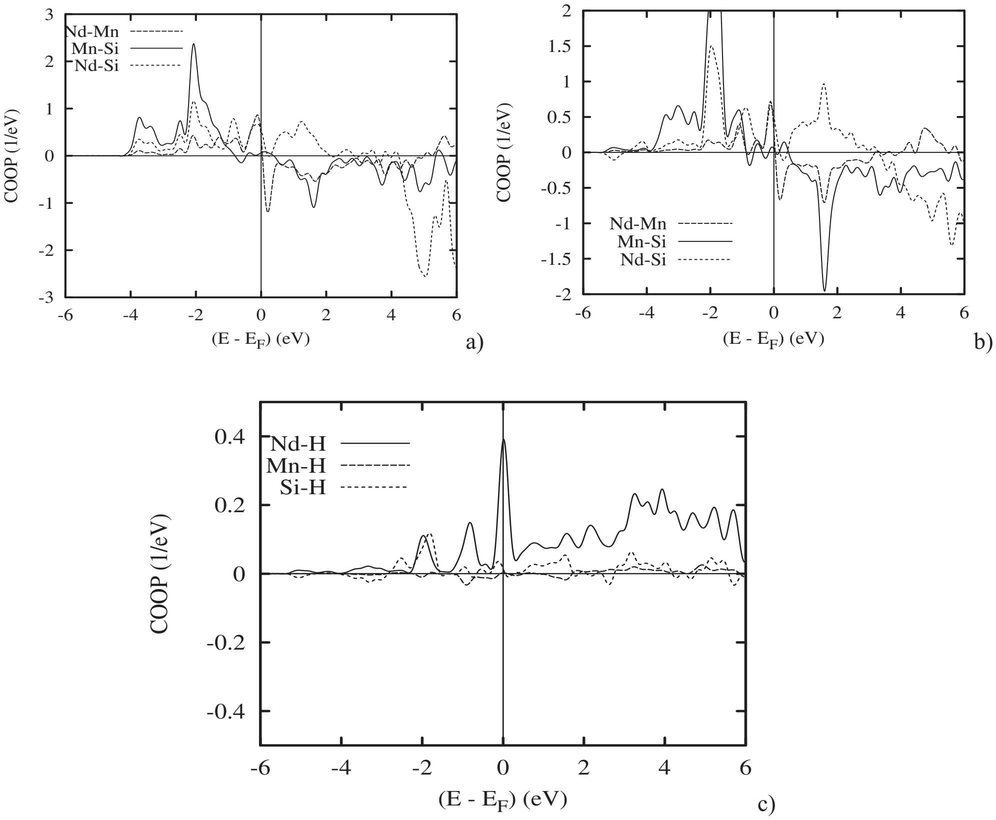

FIG. 9. Chemical bonding in NdMnSi and NdMnSiH. Nd–Mn, Mn–Si, and Nd–Si bondings in (a) NdMnSi and (b) NdMnSiH. Nd–H, Mn–H, and Si–H bondings in the hydride. (COOP criterion: positive, negative, and zero; COOPs are relevant to bonding, antibonding, and nonbonding interactions, respectively.)

pected from the low filling of the 4f subshell, i.e., $4f^{3.4}$ and $4f^{3.3}$ for NdMnSi and its hydride with respect to theoretical $4f^4$ filling for Nd^{3+}. On the other hand 3d(Mn) states show a large $n(E_F)$ which can be correlated with an occupation ranging up to $3d^{5.5}$ and $3d^{5.6}$ for NdMnSi and its hydride with respect to a theoretical filling of five electrons for 3d(Mn) subshell. In the mean field Stoner theory of band ferromagnetism,[47] this is indicative of the instability of the system in such a NM configuration, especially for Nd and Mn in their respective 4f and 3d states. The consequence is that a finite magnetic moment should arise when SP will be allowed for (see Sec. III C 2). From Fig. 8 the lower part of the valence band (VB) is dominated by s(Si)-like states with small contribution from other constituents' itinerant states. The major part of the bonding between Nd, Mn, and Si in NdMnSi is found in the energy range −4 eV up to E_F as the PDOS skylines are similar especially between −4 and −2 eV. The effect of hydrogen insertion in the DOS picture can be found in the energy range −5.5 to −4 eV where its PDOSs have a similar shape to those of Nd. Hence one can expect a significant bonding between Nd and H.

The chemical bonding analyzed through the overlap population with the COOP criterion is illustrated in Figs. 9(a) and 9(b) for Nd–Mn, Nd–Si, and Mn–Si pair interactions and in Fig. 9(c) for Nd–H, Mn–H, and Si–H bondings. In the first two panels the VB has an overall bonding behavior with dominant Mn–Si bonding, which can be explained by the shortest interatomic distance $d_{\text{Mn–Si}}=2.467$ Å in NdMnSi and 2.492 Å in the hydride. The other bonding interactions are for Nd–Si and Nd–Mn both showing close in intensity in NdMnSi. Interestingly the Nd–Si bonding becomes dominant in the hydride concomitantly with a small decrease in the $d_{\text{Nd–Si}}$ distance from 3.090 to 3.082 Å. The stabilization of NdMnSi and its hydride by bonding pair interactions is stressed further by the COOP with H in Fig. 9(c) albeit with ten times less intensity. The Nd–H bonding is strongest because of the shortest distance $d_{\text{Nd–H}}=2.374$ Å. A weak Si–H interaction is indicated by a peak at −2 eV. Although the calculated interatomic distance is rather large ($d_{\text{Si–H}}=3.161$ Å), bonding is still possible through itinerant sp states. This is also pointed out by other works such as on $\text{RENiInH}_{1.333}$ (RE=La, Ce, Nd) hydride systems where such interactions were observed within a 3.5 Å range.[48] Lastly there are no Mn–H interactions due to their huge separation of 3.907 Å.

We further illustrate the bonding in NdMnSiH with the ELF plots shown in Fig. 10 for the plane at $y=1/4$ comprising Mn at $z=0$, Si at $z=0.188$, H at $z=1/2$, and Nd at $z=0.661$. As mentioned above the ELF is normalized between 0 and 1 for no and full localization with ELF ~ 1/2 for a free-electron-like distribution; the corresponding colors are deep blue, deep red, and grass-green, respectively. Clearly there is no localization around Mn while the strongest localization with ELF ~ 1 is for H. From this NdMnSiH can be identified as a hydride. One also finds from the green areas (ELF ~ 1/2) the expected characteristics of a metallic system. Intermediate localization is found around Si and Nd with larger extension for the former. A nonspherical distribu-

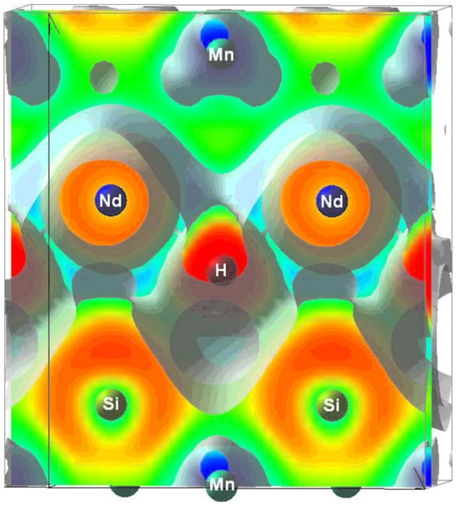

FIG. 10. (Color online) ELF for NdMnSiH: contour maps are extended over two unit cells for the plane at $y=1/4$ comprising Mn at $z=0$, Si at $z=0.188$, H at $z=1/2$, and Nd at $z=0.661$. Notice the corresponding Bader volumes around H (gray shells around atoms with an isosurface value of 0.15) toward the Nd positions.

tion is observed for the electron density of H pointing toward Nd on one hand and Si large spots pointing toward Nd and Mn. These are clear illustrations of the chemical bonding characteristics of the system described above.

A quantitative study for charge density can be performed within the Bader charge analysis which yields individual atomic charge magnitudes.[49] This meets the picture of electron localization visualized through the ELF. From the charge density obtained at self-consistent convergence of the calculations, the individual Bader charges for the atomic species of both pristine alloy and its hydride show no change for Nd which is ionic with a charge of +3.1. On the other hand, Mn charges are +0.14 and −0.02 for NdMnSi and its hydride. Silicon atoms' individual charge of −1.2 for pristine alloy is cut down to half after hydrogenation. Hydrogen atoms show a charge of −0.5 meaning that they are on the boundary between covalent and ionic bondings, namely, with Nd. This does not completely meet the theoretical study by Vajeeston *et al.* of RENiIn and their hydrides $\mathrm{RENiInH}_{1.333}$ where a charge transfer was observed for the different atomic species toward H, hence significant of a strong ionic bonding between H and the host lattice.[48] It is also important to mention that the Bader volumes are depicted in Fig. 10 with the gray shells around atoms. A visual inspection of the latter indicates the charge transfer between Nd and H, hence resulting into a strong Nd–H bonding as referred to in the COOP analysis.

2. Magnetic calculations

A FM configuration is first assumed to check for the onset of magnetic moments on the atomic species on one hand and for their nature (proper or induced) on the other hand. Further the total energy of such FM configurations will be checked against that of the AFM ones for identifying the ground state. The results are given in Table III for the magnetic moments and for the energetics.

TABLE III. Calculated magnetic moments (spin only) in NdMnSi and NdMnSiH for FM and AFM configurations.

	NdMnSi		NdMnSiH	
	FM (μ_B mol^{-1})	AFM (μ_B mol^{-1})	FM (μ_B mol^{-1})	AFM (μ_B mol^{-1})
Nd	3.526	±3.334	3.161	±3.190
Mn	1.920	±2.721	2.060	±2.611
Si	−0.07	±0.008	−0.065	±0.010
H			−0.003	±0.002
Total	5.38	±6.06	5.15	±5.79
$\Delta E_{\text{FM-NM}}$ eV mol^{-1}	−1.557		−1.528	
$\Delta E_{\text{AFM-FM}}$ eV mol^{-1}	−0.009		−0.023	

The calculations show that SP stabilizes both systems by ~1.5 eV mol^{-1} with respect to the first assumed NM configuration. This large stabilization energy ΔE, namely, with respect to $\Delta E_{\text{AFM-FM}}$, is due to magnetic exchange allowing for the onset of local magnetic moments. Then when the calculations are done on the AFM configuration the compounds further stabilize (Table III) with a larger magnitude for NdMnSiH than for NdMnSi. This is concomitant with a larger total magnetic moment in the AFM configurations for both compounds. NdMnSiH has lower magnitudes of magnetic moment which is connected with the Nd–H chemical bonding leading to a slight lowering of the Nd moment magnitude. The negligible moments on Si and H and their negative signs are clearly of induced character due to the mixing of their valence states with those of the magnetically polarized atoms, i.e., Nd and Mn. A peculiar result is observed for Mn whose moment is enhanced for NdMnSiH in the FM configuration. Further the Mn moment increases within the hydride when the AFM ordering is established. The expansion of the lattice upon the H insertion is in favor of a larger isolation of Mn and its magnetic moment enhancement as it can be inferred from the ELF maps of the hydride (Fig. 10) but the peculiar feature is the strong enhancement of the Mn moment in the AFM configuration which can be due to the isolated character as well as to the symmetry breaking when the AFM cell is accounted for. This mismatch of magnetic behavior between the Nd and Mn substructures upon hydriding somehow comforts the experimental findings for the ordering temperatures.

Lastly we note that calculating a hydrogen-free compound at the lattice parameters and atomic coordinates of NdMnSiH leads to a stable FM configuration with $M_{\text{Nd}}=3.52\mu_B$, $M_{\text{Mn}}=2.01\mu_B$, and $M_{\text{Si}}=-0.06\mu_B$ with $M_{\text{tot.}}=5.6\mu_B$. This stresses the picture of the role played by H bonding especially in reducing the moment on Nd and making the hydride stable in its AFM ground state. It should be noted here that the magnitude of the Nd moment is relevant to a spin-only value. The three Hund's rule starts that the orbital moment adds negatively to the spin moment for a less than half filled nf shell. With an orbital moment of $5.6\mu_B$,[50] the resulting moment on Nd of $2\mu_B$ shows better agreement with measurements.

In Fig. 11, the effects of SP are shown for the hypothetical FM configuration site and spin PDOS for NdMnSi and

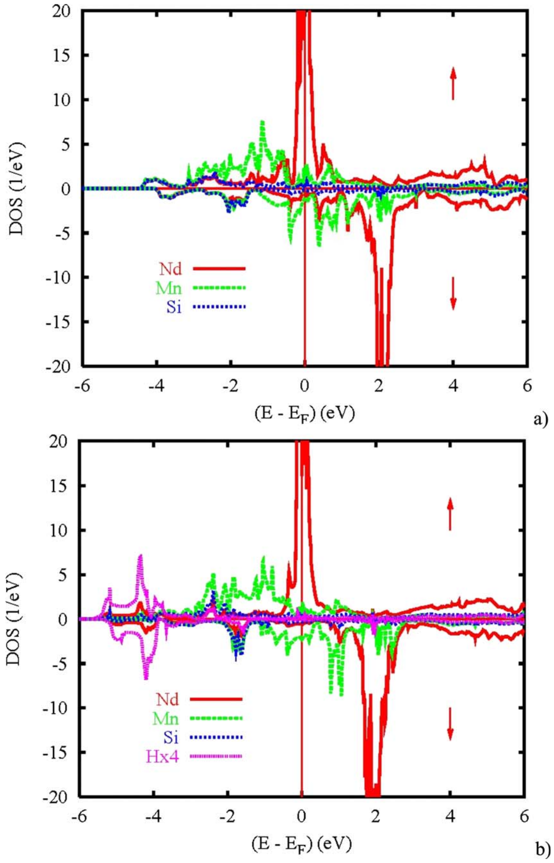

FIG. 11. (Color online) Magnetic PDOS in the hypothetic FM configuration for (a) NdMnSi and (b) NdMnSiH.

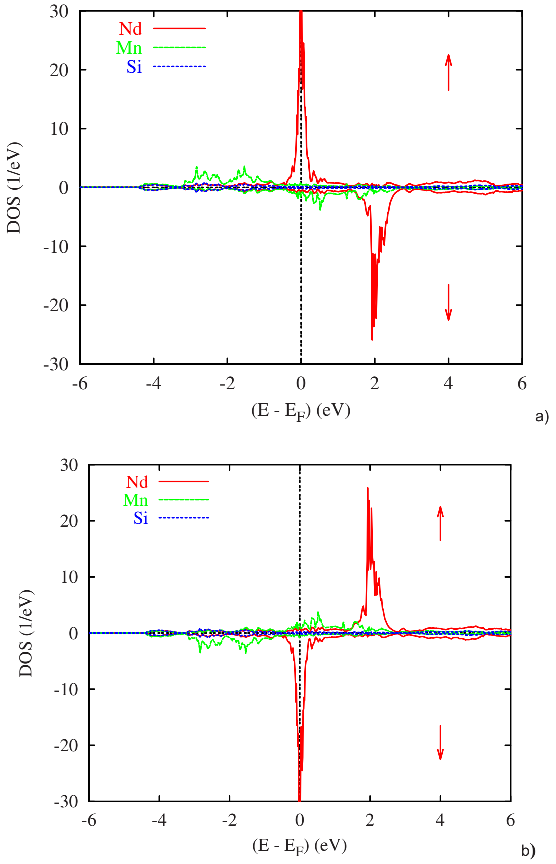

FIG. 12. (Color online) NdMnSi AFM PDOS for (a) up and (b) down spin substructures.

NdMnSiH. The large DOS at E_F, $n(E_F)$, is observed in both compounds for the spin up $(\uparrow)4f$(Nd) states. The corresponding $(\downarrow)4f$(Nd) states are centered slightly above 2 eV in the conduction band for NdMnSi and slightly below 2 eV for NdMnSiH, which is significant of the smaller moment magnitude for Nd in the latter. SP also affects $3d$(Mn) states which are interestingly less mixed with the other constituents' valence states in the hydride. This is another illustration of their isolated character as discussed above. The other aspects of the VB are similar to those discussed in the NSP DOS section. For the sake of illustrating the AFM configuration results, Figs. 12(a) and 12(b) show the AFM PDOS for (↑) and (↓) spin substructures in NdMnSi. Similar plots are obtained for the hydride. The two panels mirror each other and the resulting total magnetic moment of $\pm 6.06\mu_B$ compensates exactly.

IV. DISCUSSION

The AFM structures reported here for the hydride NdMnSiH are different from those existing for NdMnSi.[26] The first one derives from the propagation vector $\mathbf{k}=(0,0,0)$ whereas the second one is described by $\mathbf{k}=(0,0,1/2)$. But the two magnetic structures of NdMnSiH present some similarities with those of LaMnSi and CeMnSi:[26] (i) between T_{N1} and T_{N2}, the AFM arrangement of the Mn substructure is nearly similar to that evidenced for LaMnSi and (ii) below T_{N2}, the magnetic coupling between Nd and Mn substructures looks like that determined at 1.4 K for CeMnSi. Other comparison concerns the evolution of the Néel temperatures T_{N1} and T_{N2} in the sequence NdMnSi→NdMnSiH: T_{N1} increases strongly whereas T_{N2} decreases. As T_{N1} concerns the AFM ordering of the Mn substructure, its increase is correlated with the decrease in the intralayer distances $d_{\text{Mn–Mn}}$ in this sequence from 2.901(5) to 2.847(5) Å. It is well known, using the Bethe–Slater curve,[51] that the decrease in the distance between two Mn atoms reinforces their AFM interaction. It is more difficult to explain the decrease in T_{N2} in the considered sequence. Nevertheless, the electronic structure calculation performed on the hydride NdMnSiH (Fig. 10) reveals strong bonding between Nd and H atoms. This plays an important role on the magnetic properties of the Nd substructure in the hydride.

In order to explain the magnetic properties of the compounds REMn*X* and REMn*X*H, it is necessary to consider three main types of exchange interactions: Mn–Mn, RE–Mn, and RE–RE.[26,52,53] In NdMnSiH, the high value of the Néel temperature T_{N1} of the Mn substructure clearly indicates that the Mn–Mn AFM interaction is strong and predominant. The temperature dependence of the Mn ordered magnetic moment (Fig. 7) can been self-consistently calculated using a Brillouin function to obtain its magnetization in its own molecular field. The two parameters for this calculation are the Mn moment determined at low temperature $\mu_{\text{LT}}(\text{Mn}) = 2.80(5)\mu_B$ and the molecular field constant $\lambda_{\text{Mn–Mn}}$. The first parameter is fixed by the experimental data and the second one is determined using T_{N1} and $\mu_{\text{LT}}(\text{Mn})$. In NdMnSiH,

$T_{N1}=565$ K corresponds to $\lambda_{\text{Mn–Mn}}=147$ T/μ_B and the mean molecular field seen by Mn is $\lambda_{\text{Mn–Mn}}\mu_{\text{Mn}}(T)$. As shown in Fig. 7 we obtain a good estimation which reproduces the characteristic feature of the temperature dependence of the refined Mn moment. In this calculation, we neglect any influence of Nd on the Mn substructure below T_{N2}. This estimation confirms that the Mn–Mn interaction is predominant.

Regarding the Nd ordered moment, its temperature dependence behavior does not look like that of the Mn one and especially, it exhibits an inflection point around 40 K (Fig. 7). This unusual shape has already been observed in compounds with two different magnetic substructures such as the pyrochlore $Gd_2Mo_2O_7$,[54] the Laves phase hydrides $REMn_2H_{4.5}$,[55] and the ternary germanides $Tb_3Mn_4Ge_4$ (Ref. 56) and TmMnGe.[57] If we try to fit $\mu_{\text{Nd}}(T)$ by only considering the Nd substructure in its own molecular field without any Nd—Mn exchange interaction, the fit, which only depends on $\mu_{\text{LT}}(\text{Nd})=1.88(5)\mu_B$ and $T_{N2}=100(5)$ K, is bad. In particular, there is no inflection point. The explanation of the temperature dependence of the Nd moment is thus more complicated and we need to take into account the Mn–Nd interaction. This is corroborated by the reorientation of the Mn substructure which occurs at T_{N2} when the Nd substructure presents an AFM ordering, indicating that the Mn and Nd sublattices are in interaction. We can describe the Nd moments in the molecular field of the Mn substructure, neglecting any influence of Nd on the Mn substructure. The energy states of Nd are split in five Kramers doublets by the crystal field and if we make the hypothesis that only the ground Kramers doublet is occupied, the temperature dependence of the Nd moment is calculated through the formula

$$\mu_{\text{Nd}}(T) = 1/2g\mu_B \tanh[g\mu_B\lambda_{\text{Nd–Mn}}\mu_{\text{Mn}}/2k_BT],$$

corresponding to a spin $S'=1/2$ and where $\lambda_{\text{Nd–Mn}}$ is the molecular field constant in (T/μ_B) units and g the Landé factor in the direction of the molecular field. We have fitted $\mu_{\text{Nd}}(T)$ using the above formula, taking the experimental data for $1/2g\mu_B=\mu_{\text{LT}}(\text{Nd})$ and the calculated data for $\mu_{\text{Mn}}(T)$ and adjusting the molecular field constant $\lambda_{\text{Nd–Mn}}$. With the value $\lambda_{\text{Nd–Mn}}=8.4$ T/μ_B corresponding to a molecular field of 23.6 T on the Nd site, we obtain a very good fit of the experimental data below 100 K as shown in Fig. 7. This result suggests that the Nd–Mn interaction is likely greater than the Nd–Nd interaction below T_{N2}. Nevertheless, this fit is not good any more above T_{N2} which suggests that in this temperature range the Nd–Mn interaction is largely weaker than for $T<T_{N2}$. First, to explain why the Nd–Mn interaction is weak above T_{N2} we can consider the following structural-type argument: as each Nd atom is surrounded by four nearest atoms of Mn whose moments are antiparallel two to two, the resulting interaction on Nd should be zero for any direction of the Mn moment. Thus, the Mn molecular field seen by the Nd atom is zero in first approximation and the Nd–Mn isotropic exchange interaction also. In this case, if the Nd–Mn interaction is weak (only anisotropic coupling) as well as the Nd–Nd interaction (RKKY type), then the Nd substructure does not order magnetically. Second, below T_{N2}, the AFM arrangement of the Mn substructure determined by neutron diffraction still leads to the cancellation of the Nd–Mn interaction on Nd. But one hypothesis to understand the increase in the Nd–Mn coupling below T_{N2} is to consider the occurrence of a slight canting on the Mn atoms which would imply that the moments of the four Mn surrounding a Nd atom do not exactly compensate for each other. The occurrence of a nonzero molecular field on the Nd atom could induce the rare earth polarization at T_{N2} and the Mn-substructure reorientation. We notice that no canting is observed on the neutron data but a small FM component can be too weak to be seen in neutron diffraction. Moreover, a small canting on the Mn atoms could also explain the weak FM component seen on the magnetic isotherms below 100 K. It is noteworthy that a small lattice distortion yielding two sets of Nd–Mn interatomic distances could also explain the onset of isotropic Nd–Mn coupling even if this effect is not observed either in neutron diffraction with its resolution. These hypotheses can provide some explanations for the Nd magnetic behavior but it is possible that it requires more sophisticated exchange interaction models.

In NdMnSiH, the value of the Mn moment, $2.80(5)\mu_B$ at 1.4 K, is smaller than that reported for NdMnSi [$2.97(5)\mu_B$ at 2 K][26] or NdMnGe [$3.17(6)\mu_B$ at 2 K][52] but higher than those existing in $NdMn_2Si_2$ ($1.61\mu_B$ at 1.6 K)[44] or $NdMn_2Ge_2$ ($2.7\mu_B$ at 2 K).[58] It has already been shown that, in the families of compounds REMnX and $REMn_2X_2$, the Mn moment value is strongly correlated with the $d_{\text{Mn–Mn}}$ distance and to the type of magnetic interaction for the Mn–Mn intralayer coupling. For $d_{\text{Mn–Mn}}$ intralayer larger than approximately 2.86 Å and/or Mn moment greater than approximately $2.5\mu_B$ the Mn–Mn intralayer coupling is AFM or dominant AFM (mixed). In the inverse case, the Mn moments within the (001) planes are ferromagnetically coupled. Regarding NdMnSiH, the Mn–Mn intralayer coupling is AFM; the Mn moment value is indeed higher than $2.5\mu_B$ but the $d_{\text{Mn–Mn}}$ (2.847 Å) is slightly weaker than the critical value. Therefore, the hydride deviates from this model as other compounds previously reported.[59] Thus, another criterion based on the $d_{\text{Mn-}X}$ distance has been introduced to better account for the Mn-substructure magnetic behavior. Indeed, Mn being surrounding by four X atoms as nearest neighbors, the overlapping of the X and Mn orbitals should greatly influence the filling and the shape of the $3d$(Mn) band. The strong and dominant Mn–Si bonding has been confirmed by the electronic calculations. If one studies the variation of the $d_{\text{Mn-}X}$ relative contraction $\Delta_{\text{Mn-}X}(\%)=100(d_{\text{Mn-}X}-\Delta r)/\Delta r$, where Δr is the sum of the radii of the elements, one finds a strong correlation between this variation and the Mn moment value. Figure 13 shows the plot of μ_{Mn} versus $\Delta_{\text{Mn-}X}$ deduced, in particular, from the single crystal x-ray diffraction studies as described previously in Ref. 56. It clearly shows that a strong contraction leads to a low value of μ_{Mn} and to FM Mn–Mn in plane interactions and a weak contraction to a high value of μ_{Mn} connected to AFM or mixed Mn–Mn in plane coupling. Both ranges are delimitated by the critical values $\mu_{\text{Mn}}\approx 2.5\mu_B$ and the relative contraction $\Delta_{\text{Mn-}X}\approx -6.2\%$. For NdMnSiH, we find $\mu_{\text{Mn}}=2.80(5)\mu_B$, a relative contraction $\Delta_{\text{Mn-}X}=-5.0\%$, and AFM Mn–Mn in plane interaction: the criterion previously

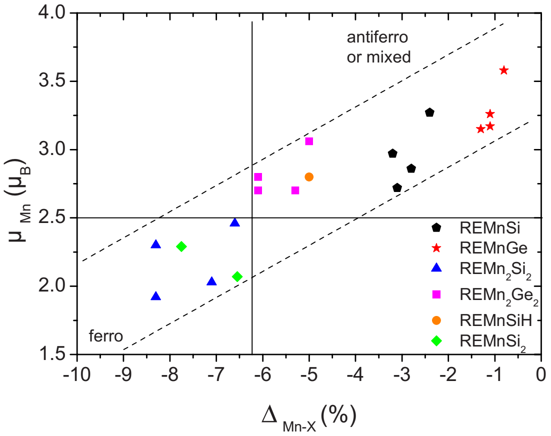

FIG. 13. (Color online) Mn moment value vs $\Delta_{\text{Mn-}X}$ (see text) in NdMnSiH and some REMnX, REMn$_2X_2$, and REMnSi$_2$ compounds (X=Si or Ge).

described nicely accounts for the Mn moment value and, as the $\Delta_{\text{Mn-}X}$ value is very close to those of the REMn$_2$Ge$_2$ compounds, it explains why their Mn moments are also very close.

In NdMnSiH, the magnetic moment of Nd is found to be 1.88(5)μ_B at 1.4 K, which is lower than in NdMnSi [2.59(1)μ_B at 2 K][26] or NdMn$_2$Si$_2$ [2.83(4)μ_B at 1.6 K][44] but about the same as in NdMnSi$_2$ [1.80(7)μ_B at 2 K].[46] The electronic and magnetic calculations (see Sec. III C) have shown that the chemical bonding between Nd and H was strong and the strongest electron localization was for H. This leads to a slight lowering of the Nd moment value and it illustrates the role played by the H insertion.

V. CONCLUSION

The crystal and magnetic structures of NdMnSiH have been determined by a neutron diffraction study. It confirms that the H atoms are inserted in the [Nd$_4$] tetrahedral sites which are fully occupied. It also shows, in accordance with the magnetization and specific heat measurements, that the Mn AFM ordering temperature occurs at very high temperature since $T_{N1}=565(5)$ K. The Nd substructure orders antiferromagnetically at $T_{N2}=100(5)$ K and, at the same time, a spin reorientation of the Mn substructure occurs.

We notice that the hydrogenation of NdMnSi does not change the nature of the magnetic ordering since in both compounds NdMnSi and NdMnSiH, the Mn and Nd substructures order antiferromagnetically. Nevertheless, it is noteworthy that the T_{N1} Néel temperature has much increased from 280 to 565 K after hydrogenation, which is linked to the decrease in the intralayer distance $d_{\text{Mn–Mn}}$ from 2.901 to 2.847 Å and so the increase in the Mn–Mn exchange interaction. In an opposite way, the Nd ordering temperature has decreased from 185 to 100 K as well as the value of the Nd moment from 2.59μ_B to 1.88μ_B at 1.4 K. Moreover, the propagation vector is $\mathbf{k}=(0\ 0\ 1/2)$ in NdMnSi and $\mathbf{k}=(0\ 0\ 0)$ in the hydride: as a consequence, the Mn–Mn and the Nd–Nd nearest interplane interactions are AFM and FM, respectively, in NdMnSi and are opposite in NdMnSiH. On the contrary, the Mn–Mn and the Nd–Nd nearest intraplane interactions are AFM and FM, respectively, in both compounds. Thus the magnetic structure and the ordering temperature have much changed after the hydrogenation of NdMnSi. Band structure calculations have been done in order to address the role of the Mn–Mn, Nd–Nd, and Nd–Mn exchange interactions in the thermal evolution of the Mn and Nd moments which are calculated to be in agreement with the experiments. Also, the influence of the strong bonding between Nd and H on the magnetic properties of the hydride has been discussed using the chemical bonding and electron localization mapping.

ACKNOWLEDGMENTS

The authors would like to thank R. Decourt for his assistance during the specific heat measurements. B. Chevalier thanks the European Science Foundation (ECOM-COST action P16) for financial support. The authors from ICMCB and LLB are indebted to the Conseil Régional d'Aquitaine for financial support; especially S. Tencé for a Ph.D. stipend. Finally, B. Chevalier, E. Gaudin, and R. Pöttgen are indebted to EGIDE and DAAD for research grants within the PROCOPE programs (Grant Nos. 11457RD, 17841TJ and D/0502176).

[1] B. I. Zimmer, W. Jeitschko, J. H. Albering, R. Glaum, and M. Reehuis, J. Alloys Compd. **229**, 238 (1995).
[2] A. T. Nientiedt, W. Jeitschko, P. G. Pollmeier, and M. Brylak, Z. Naturforsch., B: Chem. Sci. **52**, 560 (1997).
[3] P. Quebe, L. J. Terbüchte, and W. Jeitschko, J. Alloys Compd. **302**, 70 (2000).
[4] R. Pöttgen, W. Hönle, and H. G. von Schnering, *Phosphides: Solid-State Chemistry, in Encyclopedia of Inorganic Chemistry*, 2nd ed. (J. Wiley, Chichester, 2005), Vol. VII, p. 4255.
[5] Y. Kamihara, H. Hiramatsu, M. Hirano, R. Kawamura, H. Yanagi, T. Kamiya, and H. Hosono, J. Am. Chem. Soc. **128**, 10012 (2006).
[6] S. Lebègue, Phys. Rev. B **75**, 035110 (2007).
[7] M. Tegel, I. Schellenberg, R. Pöttgen, and D. Johrendt, Z. Naturforsch., B: Chem. Sci. **63**, 1057 (2008).
[8] T. Watanabe, H. Yanagi, T. Kamiya, Y. Kamihara, H. Hiramatsu, M. Hirano, and H. Hosono, Inorg. Chem. **46**, 7719 (2007).
[9] M. Tegel, D. Bichler, and D. Johrendt, Solid State Sci. **10**, 193 (2008).
[10] Y. Kamihara, T. Watanabe, M. Hirano, and H. Hosono, J. Am. Chem. Soc. **130**, 3296 (2008).
[11] H. Takahashi, K. Igawa, K. Arii, Y. Kamihara, M. Hirano, and H. Hosono, Nature (London) **453**, 376 (2008).
[12] G. F. Chen, Z. Li, D. Wu, G. Li, W. Z. Hu, J. Dong, P. Zheng, J. L. Luo, and N. L. Wang, Phys. Rev. Lett. **100**, 247002 (2008).
[13] G. F. Chen, Z. Li, D. Wu, J. Dong, G. Li, W. Z. Hu, P. Zheng, J. L. Luo, and N. L. Wang, Chin. Phys. Lett. **25**, 2235 (2008).
[14] X. H. Chen, T. Wu, D. Wu, R. H. Liu, H. Chen, and D. F. Fang, Nature (London) **453**, 761 (2008).
[15] H. Kito, H. Eisaki, and A. Iyo, J. Phys. Soc. Jpn. **77**, 063707 (2008).
[16] H. Lincke, R. Glaum, V. Dittrich, M. Tegel, D. Johrendt, W. Hermes, M. H. Möller, T. Nilges, and R. Pöttgen, Z. Anorg. Allg. Chem. **634**, 1339 (2008).
[17] B. Chevalier, E. Gaudin, F. Weill, and J.-L. Bobet, Intermetallics **12**, 437 (2004).
[18] B. Chevalier and S. F. Matar, Phys. Rev. B **70**, 174408 (2004).
[19] B. Chevalier, M. Pasturel, J.-L. Bobet, and O. Isnard, Solid State Commun. **134**, 529 (2005).
[20] B. Chevalier, S. F. Matar, J. Sanchez Marcos, and J. Rodriguez Fernandez, Physica B **795**, 378 (2006).
[21] B. Chevalier, S. F. Matar, M. Ménétrier, J. Sanchez Marcos, and J. Rodriguez Fernandez, J. Phys.: Condens. Matter **18**, 6045 (2006).
[22] B. Chevalier, E. Gaudin, S. Tencé, B. Malaman, J. Rodriguez Fernandez, G. André, and B. Coqblin, Phys. Rev. B **77**, 014414 (2008).
[23] S. Tencé, G. André, E. Gaudin, and B. Chevalier, J. Phys.: Condens. Matter **20**, 255239 (2008).
[24] R. Pöttgen and D. Johrendt, Z. Naturforsch., B: Chem. Sci. **63**, 1135

(2008).
[25] S. F. Matar, Phys. Rev. B **75**, 104422 (2007).
[26] R. Welter, G. Venturini, and B. Malaman, J. Alloys Compd. **206**, 55 (1994).
[27] J.-L. Bobet, S. Pechev, B. Chevalier, and B. Darriet, J. Alloys Compd. **267**, 136 (1998).
[28] J. Rodriguez-Carvajal, Satellite Meeting for the 15th Congress of IUCr on Powder Diffraction, Toulouse, France, 1990 (unpublished), p. 127.
[29] V. F. Sears, Neutron News **3**, 26 (1992).
[30] A. J. Freeman and J. P. Desclaux, J. Magn. Magn. Mater. **12**, 11 (1979).
[31] P. Hohenberg and W. Kohn, Phys. Rev. **136**, 864 (1964).
[32] W. Kohn and L. J. Sham, Phys. Rev. **140**, 1133 (1965).
[33] A. R. Williams, J. Kübler, and C. D. Gelatt, Phys. Rev. B **19**, 6094 (1979).
[34] V. Eyert, *The Augmented Spherical Wave Method—A Comprehensive Treatment*, Lecture Notes on Physics Vol. 719 (Springer, Berlin, 2007).
[35] S. H. Vosko, L. Wilik, and M. Nusair, Can. J. Phys. **58**, 1200 (1980).
[36] S. F. Matar, J. F. Riecken, B. Chevalier, R. Pöttgen, A. F. Al Alam, and V. Eyert, Phys. Rev. B **76**, 174434 (2007).
[37] V. I. Anisimov, J. Zaanen, and O. K. Andersen, Phys. Rev. B **44**, 943 (1991).
[38] A. M. N. Niklasson, J. M. Wills, M. I. Katsnelson, I. A. Abrikosov, O. Eriksson, and B. Johannsson, Phys. Rev. B **67**, 235105 (2003).
[39] I. A. Nekrasov, K. Held, N. Blümer, A. I. Poteryaev, V. I. Anisimov, and D. Vollhardt, Eur. Phys. J. B **18**, 55 (2000).
[40] R. Hoffmann, Angew. Chem., Int. Ed. Engl. **26**, 846 (1987).
[41] A. D. Becke and K. E. Edgecombe, J. Chem. Phys. **92**, 5397 (1990).
[42] J. E. Bonnet and J. N. Daou, J. Appl. Phys. **48**, 964 (1977).
[43] S. Kervan, Y. Elerman, and M. Acet, J. Alloys Compd. **335**, 70 (2002).
[44] R. Welter, G. Venturini, D. Fruchart, and B. Malaman, J. Alloys Compd. **191**, 263 (1993).
[45] D. Givord and D. Courtois, J. Magn. Magn. Mater. **196–197**, 684 (1999).
[46] B. Malaman, G. Venturini, L. Pontonnier, and D. Fruchart, J. Magn. Magn. Mater. **86**, 349 (1990).
[47] J. Kübler and V. Eyert, in *Electronic Structure Calculations, Electronic and Magnetic Properties of Metals and Ceramics*, edited by K. H. J. Buschow (VCH, Weinheim, 1992), pp. 1–145.
[48] P. Vajeeston, P. Ravindran, R. Vidya, K. Kjekshus, H. Fjellvåg, and V. A. Yartys, Phys. Rev. B **67**, 014101 (2003).
[49] R. F. W. Bader, *Atoms in Molecules–A Quantum Theory* (Oxford University Press, Oxford, 1990).
[50] O. Eriksson, M. S. S. Brooks, and B. Johansson, Phys. Rev. B **41**, 7311 (1990).
[51] L. Néel, Ann. Phys. **5**, 233 (1936).
[52] R. Welter, G. Venturini, E. Ressouche, and B. Malaman, J. Alloys Compd. **228**, 59 (1995).
[53] R. Welter, I. Ijjaali, G. Venturini, and B. Malaman, J. Alloys Compd. **265**, 196 (1998).
[54] I. Mirebeau, A. Apetrei, I. Goncharenko, D. Andreica, P. Bonville, J. P. Sanchez, A. Amato, E. Suard, W. A. Crichton, A. Forget, and D. Colson, Phys. Rev. B **74**, 174414 (2006).
[55] I. N. Goncharenko, I. Mirebeau, A. V. Irodova, and E. Suard, Phys. Rev. B **59**, 9324 (1999).
[56] G. Venturini, B. Malaman, and E. Ressouche, J. Alloys Compd. **248**, 101 (1997).
[57] V. Klosek, A. Vernière, B. Ouladdiaf, and B. Malaman, J. Magn. Magn. Mater. **256**, 69 (2003).
[58] R. Welter, G. Venturini, E. Ressouche, and B. Malaman, J. Alloys Compd. **218**, 204 (1995).
[59] R. Welter, B. Malaman, and G. Venturini, Solid State Commun. **108**, 933 (1998).
[60] J. F. Berar and P. Lelann, J. Appl. Crystallogr. **24**, 1 (1991).